An interface force measurements-based substructure identification and an analysis of the uncertainty propagation

Tadej Kranjc[1], Janko Slavič*[2], Miha Boltežar[2]

November 22, 2014

Cite as:

Kranjc, T., Slavič, J. and Boltežar, M., **An interface force measurements-based substructure identification and an analysis of the uncertainty propagation**, Mechanical Systems and Signal Processing, DOI: 10.1016/j.ymssp.2014.11.005

---

[1] Ydria Motors d.o.o., Podskrajnik 16, 1380 Cerknica, Slovenia-EU.

[2] Faculty of Mechanical Engineering, University of Ljubljana, Aškerčeva 6, 1000 Ljubljana, Slovenia-EU.

* Corresponding author: Miha Boltežar, miha.boltezar@fs.uni-lj.si, +386 1 4771 608

Abstract

Substructure-decoupling techniques are used to identify a substructure as a stand-alone system while it is coupled to a complex structure (an assembly of substructures). These recently introduced techniques can be used for various applications, *e.g.*, when the substructure cannot be measured separately from the complex structure, when modal testing methods are not appropriate due to the limits of the measurement equipment and for vibration-control techniques. The complex structure consists of the unknown substructure and the remaining structure. A drawback of the available substructure-decoupling techniques is that they require a model of the remaining substructure. However, when the model cannot be calculated or (experimentally) identified, the substructure-decoupling techniques cannot be used. In this article a new approach is presented

that does not require a model of the remaining substructure, but is based on an experimental identification of the interface forces. As an illustration, the subsystem identification is introduced on a generalized mass-spring-damper system. To research the application possibilities for real situations, complex structures with beam-like coupling elements are investigated. The sensitivity of the approach to experimental errors was researched using an uncertainty propagation analysis. The article includes numerical and experimental test cases.

Keywords: substructure decoupling, interface force identification, uncertainty propagation

1 Introduction

Substructure techniques were developed to characterize complex structures that are assembled from several substructures (parts) [1–3]. In the field of substructure-coupling techniques each of the substructures can first be analyzed independently of the others. Then, the obtained results are used to calculate the dynamical behavior of the complete complex structure [1, 2]. Substructure-coupling techniques can be used, *e.g.*, to reduce the computational time in the field of finite-element methods (FEMs) or to combine theoretically and experimentally derived models [1]. In this research the inverse problem is considered, where a substructure is identified as a stand-alone system while it is coupled to a complex structure. These recently introduced methods are termed substructure-decoupling techniques [4–7] and can be used to identify the substructure's model when it cannot be disassembled or it cannot be measured independently of the complex structure, *e.g.*, a fixture is needed for the testing [6]. Further, substructure techniques can be used in structural monitoring and vibration-control [6].

In the field of substructure-decoupling techniques the complex structure is usually divided into the unknown and the remaining substructures. The result of the substructure-decoupling technique is a model of the unknown substructure, which is identified from the complex structure. The substructure-decoupling techniques can be classified as the inverse and the direct decoupling techniques [8]. The inverse techniques are based on coupling equations, that are rearranged in such a way that the model of the unknown substructure is isolated [8]. Examples of the inverse techniques are the impedance [7, 9, 10] and the mobility [4, 7, 10] substructure-decoupling techniques. The direct decoupling techniques are based on the adding of a fictitious subsystem to the model of the complex structure, that is the negative of the residual substructure [6, 8, 11].

It is a common feature of all the available decoupling techniques that they require a dynamical model of the complex and the remaining substructures. The model of the complex structure is identified experimentally and the model of the remaining substructure is calculated or experimentally identified. A drawback of the substructure-decoupling techniques is that the calculation or identification of the remaining substructure's model requires an additional effort. When the remaining substructure is too complicated to be calculated or experimentally identified, the substructure-decoupling techniques cannot be used.

In this research a new approach to linear substructure decoupling is introduced that does not require a model of the remaining substructure. This approach is based on measuring the interface forces [1]. The interface forces of the complex structures usually cannot be measured directly; therefore, an identification is made. In this article two types of dynamical systems are analyzed. As an illustration, the proposed approach is considered on a mass-spring-damper system. To show the application possibilities of the proposed approach for real structures, this research considers complex structures with beam-like coupling elements, *i.e.*, structures where there is a beam in the region of the coupling degrees of freedom (many real structures contain beam-like components in their assembly). The research includes an uncertainty propagation analysis of the proposed approach. This approach was also validated by numerical simulations and experimental tests.

The article is organized as follows: Section 2 introduces the responses of the complex structure and substructures. Section 3 describes the approach to substructure decoupling. This is followed by the theory of error analysis in Section 4. The case studies are presented in Sections 5 and 6. The conclusion follows in Section 7.

2 The responses of the complex structure and the coupled substructures

The substructure decoupling will be considered for the complex structure AB (Fig. 1a) that is assembled from the substructures A and B. It is assumed that the considered systems are linear and time invariant. In this article all the quantities are functions of frequency, except for the constants and integers. The subscripts a, b and c correspond to the substructures A, B and the coupling degrees of freedom (DOF), respectively. The structure AB is excited with the external excitation forces $\mathbf{f}_{\mathrm{a}}$ and $\mathbf{f}_{\mathrm{b}}$ (Fig. 1a). The response for the structure

AB is defined as [1, 5, 12]:

$$\begin{bmatrix} \mathbf{u}_\mathrm{a} \\ \mathbf{u}_\mathrm{c} \\ \mathbf{u}_\mathrm{b} \end{bmatrix} = \underbrace{\begin{bmatrix} \mathbf{H}_{\mathrm{aa}}^{\mathrm{AB}} & \mathbf{H}_{\mathrm{ab}}^{\mathrm{AB}} \\ \mathbf{H}_{\mathrm{ca}}^{\mathrm{AB}} & \mathbf{H}_{\mathrm{cb}}^{\mathrm{AB}} \\ \mathbf{H}_{\mathrm{ba}}^{\mathrm{AB}} & \mathbf{H}_{\mathrm{bb}}^{\mathrm{AB}} \end{bmatrix}}_{\mathbf{H}^{\mathrm{AB}}} \begin{bmatrix} \mathbf{f}_\mathrm{a} \\ \mathbf{f}_\mathrm{b} \end{bmatrix} \tag{1}$$

where $\mathbf{u}_\mathrm{a}$ and $\mathbf{u}_\mathrm{b}$ are the responses that correspond to the internal DOF of the substructures A and B, respectively. $\mathbf{u}_\mathrm{c}$ is the response of the coupling DOF. $\mathbf{H}^{\mathrm{AB}}$ is the frequency-response-function (FRF) matrix of the complex structure AB (without the elements that correspond to the coupling DOF). Using the interface forces $\mathbf{f}_\mathrm{c}^{\mathrm{A}}$ (Fig. 1b) the response of the coupled substructure A (Fig. 1b) can be written as [5]:

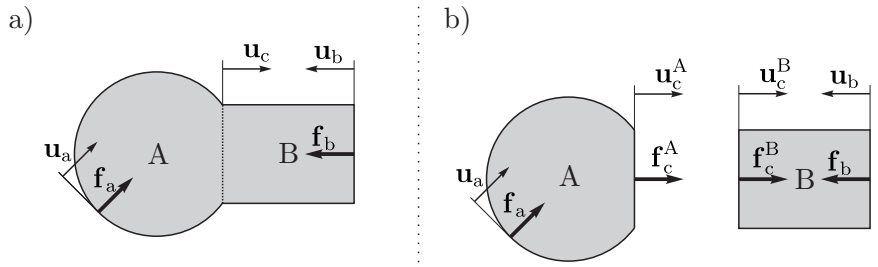

Fig. 1: a) The complex structure AB; b) The coupled substructures A and B

$$\begin{bmatrix} \mathbf{u}_\mathrm{a} \\ \mathbf{u}_\mathrm{c}^\mathrm{A} \end{bmatrix} = \underbrace{\begin{bmatrix} \mathbf{H}_{\mathrm{aa}}^{\mathrm{A}} & \mathbf{H}_{\mathrm{ac}}^{\mathrm{A}} \\ \mathbf{H}_{\mathrm{ca}}^{\mathrm{A}} & \mathbf{H}_{\mathrm{cc}}^{\mathrm{A}} \end{bmatrix}}_{\mathbf{H}^{\mathrm{A}}} \begin{bmatrix} \mathbf{f}_\mathrm{a} \\ \mathbf{f}_\mathrm{c}^\mathrm{A} \end{bmatrix} \tag{2}$$

where $\mathbf{H}^{\mathrm{A}}$ is the FRF matrix of the substructure A. Using the interface forces $\mathbf{f}_\mathrm{c}^{\mathrm{B}}$ the response of the coupled substructure B can be written as [5]:

$$\begin{bmatrix} \mathbf{u}_\mathrm{c}^\mathrm{B} \\ \mathbf{u}_\mathrm{b} \end{bmatrix} = \underbrace{\begin{bmatrix} \mathbf{H}_{\mathrm{cc}}^{\mathrm{B}} & \mathbf{H}_{\mathrm{cb}}^{\mathrm{B}} \\ \mathbf{H}_{\mathrm{bc}}^{\mathrm{B}} & \mathbf{H}_{\mathrm{bb}}^{\mathrm{B}} \end{bmatrix}}_{\mathbf{H}^{\mathrm{B}}} \begin{bmatrix} \mathbf{f}_\mathrm{c}^\mathrm{B} \\ \mathbf{f}_\mathrm{b} \end{bmatrix} \tag{3}$$

where $\mathbf{H}^{\mathrm{B}}$ is the FRF matrix of the substructure B.

When the substructures A and B are assembled, the compatibility and equilibrium conditions are satisfied for the coupling DOF. The compatibility of the displacements is written as [1, 4, 5]:

$$\mathbf{u}_\mathrm{c} = \mathbf{u}_\mathrm{c}^\mathrm{A} = \mathbf{u}_\mathrm{c}^\mathrm{B} \tag{4}$$

and the force equilibrium between the substructures A and B is written as [1, 4, 5]:

$$\mathbf{f}_\mathrm{c}^\mathrm{A} + \mathbf{f}_\mathrm{c}^\mathrm{B} = 0 \tag{5}$$

3 The substructure-decoupling procedure

This article introduces a linear substructure-decoupling technique to identify the substructure B as a stand-alone structure while it is coupled to the structure AB (Fig. 1b). The proposed approach is based on the decoupling technique presented by Sjövall and Abrahamsson [4] and further developed by Voormeeren and Rixen [5]. This technique requires a response model A for the interface force identification. With the proposed technique the interface forces $\mathbf{f}_\mathrm{c}^\mathrm{B}$ are identified experimentally, where the mathematical model of the substructure A is not needed. This section briefly describes the general procedure for the proposed substructure decoupling. More details are given in the following sections. The technique is schematically shown in Fig. 2. At the ith linearly-independent excitation step the structure AB is excited with the external forces ${}_i\mathbf{f}_\mathrm{a}$ and ${}_i\mathbf{f}_\mathrm{b}$ (Section 3.1). In this research the linear independence of the excitation forces is achieved by changing the number, location and magnitudes of the excitation forces. At each excitation step the responses ${}_i\mathbf{u}_\mathrm{b}$, ${}_i\mathbf{u}_\mathrm{c}$ are measured (Section 3.1) and the interface forces ${}_i\mathbf{f}_\mathrm{c}^\mathrm{B}$ are identified (Section 3.2). After m excitation steps (m is defined in Section 3.3) the measured (identified) quantities are used to identify the substructure-B response model with the approach that is introduced in Section 3.3.

3.1 The structure excitations and response measurements

Under laboratory conditions the testing process can be controlled by exciting the structure in a similar way as in the experimental modal analysis (EMA) [1, 2, 12, 13] with a modal hammer or an electrodynamic shaker. The responses can be measured with a motion sensor (*e.g.*, a piezoelectric accelerometer or a laser vibrometer). For numerical simulations the responses are calculated using Eq. (1).

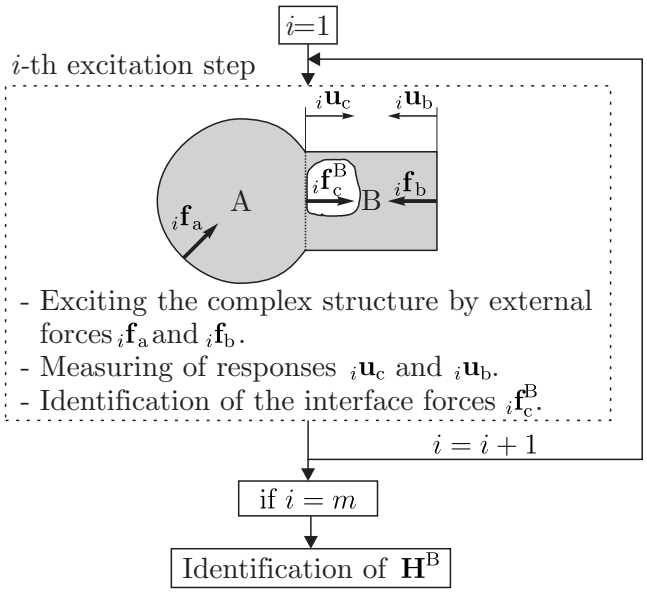

Fig. 2: The substructure-decoupling technique

3.2 The identification of the interface forces

The interface forces usually cannot be measured directly; therefore, an indirect approach has to be used. The interface force identification approaches that were presented by [4, 5] are based on Eq. (2) and (5). First, $\mathbf{f}_c^A$ is calculated from Eq. (2), which requires the FRF matrix of the substructure A. Then, $\mathbf{f}_c^B$ is calculated using Eq. (5).

In this section the interface force identification is presented that is based on the response measurements only. It does not require the FRF matrix of the substructure A. The approach will be considered on two types of substructure coupling elements (the region around the coupling DOF), *i.e.*, the springs (Fig. 3) and a beam (Fig. 4).

3.2.1 Spring element

When the coupling elements between the subsystems A and B are springs (Fig. 3), the interface force $f_c^{j,B}$, corresponding to the jth spring, is linearly dependent on the spring extension d_c^j. The interface forces are written in vector form as:

$$\mathbf{f}_{\mathrm{c}}^{\mathrm{B}} = -\left[\diagdown\mathbf{K}\diagdown\right]\,\mathbf{d}_{\mathrm{c}} \tag{6}$$

where $\left[\diagdown\mathbf{K}\diagdown\right]$ is the (diagonal) matrix of the spring's stiffness k_j and $\mathbf{d}_{\mathrm{c}}$ is a vector of d_{c}^{j}. Using the FRF matrix of the system AB the interface forces are calculated with the following equation:

$$\mathbf{f}_{\mathrm{c}}^{\mathrm{B}} = -\left[\diagdown\mathbf{K}\diagdown\right]\begin{bmatrix}\mathbf{H}_{\mathrm{c_b a}}^{\mathrm{AB}} - \mathbf{H}_{\mathrm{c_a a}}^{\mathrm{AB}} & \mathbf{H}_{\mathrm{c_b c_a}}^{\mathrm{AB}} - \mathbf{H}_{\mathrm{c_a c_a}}^{\mathrm{AB}} & \mathbf{H}_{\mathrm{c_b c_b}}^{\mathrm{AB}} - \mathbf{H}_{\mathrm{c_a c_b}}^{\mathrm{AB}} & \mathbf{H}_{\mathrm{c_b b}}^{\mathrm{AB}} - \mathbf{H}_{\mathrm{c_a b}}^{\mathrm{AB}}\end{bmatrix}\begin{bmatrix}\mathbf{f}_{\mathrm{a}}\\ \mathbf{f}_{\mathrm{c_a}}\\ \mathbf{f}_{\mathrm{c_b}}\\ \mathbf{f}_{\mathrm{b}}\end{bmatrix} \tag{7}$$

where $\mathbf{f}_{\mathrm{c_a}}$ and $\mathbf{f}_{\mathrm{c_b}}$ are external forces that excite the system AB at the points $\mathrm{c_a}$ and $\mathrm{c_b}$, respectively. $\mathbf{H}_{\mathrm{c_b a}}^{\mathrm{AB}}$ are FRFs between points $\mathrm{c}_{\mathrm{b}}^{j}$ (see Fig. 3) and internal DOF of the subsystem A. $\mathbf{H}_{\mathrm{c_a a}}^{\mathrm{AB}}$, $\mathbf{H}_{\mathrm{c_b c_a}}^{\mathrm{AB}}$, $\mathbf{H}_{\mathrm{c_a c_a}}^{\mathrm{AB}}$, $\mathbf{H}_{\mathrm{c_b c_b}}^{\mathrm{AB}}$, $\mathbf{H}_{\mathrm{c_a c_b}}^{\mathrm{AB}}$, $\mathbf{H}_{\mathrm{c_b b}}^{\mathrm{AB}}$, $\mathbf{H}_{\mathrm{c_a b}}^{\mathrm{AB}}$ are defined in a similar way as $\mathbf{H}_{\mathrm{c_b a}}^{\mathrm{AB}}$.

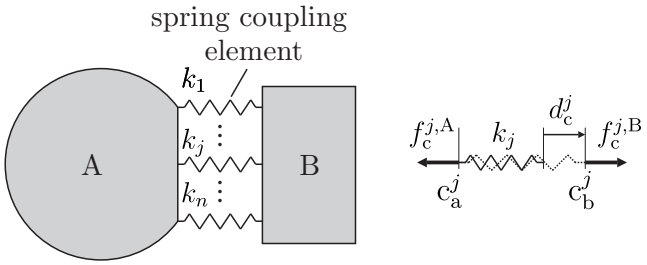

Fig. 3: The spring coupling elements

3.2.2 Beam elements

When the coupling element between the substructures A and B is a beam (Fig. 4) the interface forces are normal ($N_{x,\mathrm{c}}$) and the shear forces ($T_{y,\mathrm{c}}$, $T_{z,\mathrm{c}}$), bending ($M_{y,\mathrm{c}}$, $M_{z,\mathrm{c}}$) and torsion ($M_{x,\mathrm{c}}$) moments. However, it is assumed in this research that the coupling element is a uniform Euler-Bernoulli beam in pure planar bending in the plane xz; therefore, only the bending moments $M_{y,\mathrm{c}}$ and the shear forces $T_{z,\mathrm{c}}$ are analyzed [14]. A vector of the interface forces $\mathbf{f}_{\mathrm{c}}^{\mathrm{B}}$ for the coupling DOF c (Fig. 4) is written as:

$$\mathbf{f}_{\mathrm{c}}^{\mathrm{B}} = [-T_{z,\mathrm{c}} \quad -M_{y,\mathrm{c}}]^{\mathrm{T}} \tag{8}$$

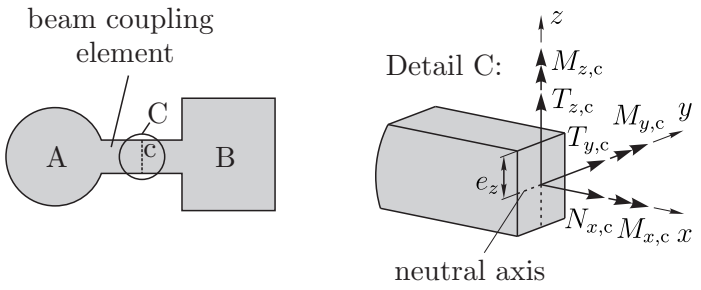

Fig. 4: The complex structure with the beam coupling element

In this section a procedure for the identification of the interface forces $\mathbf{f}_{\mathrm{c}}^{\mathrm{B}}$ is presented. The bending moments M_y result in the normal stress σ_{xx}. σ_{xx} varies linearly with the distance e_z from the neutral axis (see Fig. 4 and 8), where the normal stress and strain equal zero [15]. The normal stress at the surface is written as [15, 16]:

$$\sigma_{xx,\mathrm{s}} = \frac{M_y}{I_y}\, e_z, \tag{9}$$

where I_y is the area moment of inertia around the y-axis and e_z (Fig. 4) is the distance between the neutral axis [15] and the surface. By considering Hooke's law, the relationship between the bending moment and the strain $\varepsilon_{xx,\mathrm{s}}$ at the surface can be written as:

$$M_y = E\, \varepsilon_{xx,\mathrm{s}}\, \frac{I_y}{e_z} \tag{10}$$

where E is the Young's modulus. The shear force T_z is the first partial derivative of the bending moment with respect to x [14]:

$$T_z = \frac{\partial M_y}{\partial x} \tag{11}$$

Eq. (11) can be written in terms of the central difference formula for the first derivative [17]:

$$T_z(x) = \frac{1}{2\,h}\,\left(M_y(x+h) - M_y(x-h)\right) - \frac{h^2}{6}\,\frac{\partial^3 M_y(\xi)}{\partial x^3}; \quad h \neq 0 \tag{12}$$

where $x-h$ and $x+h$ are the nodes that are symmetrically located around x with the spacing $2\,h$. $\frac{h^2}{6}\,\frac{\partial^3 M_y(\xi)}{\partial x^3}$ is the truncation error of order $O(h^2)$, where

$x - h < \xi < x + h$. To ensure the small truncation error the spacing $2\,h$ has to be sufficiently small.

In this research the identification of the bending moment $M_{y,\mathrm{c}}$ and the shear force $T_{z,\mathrm{c}}$ is based on measuring the strain responses (with piezoelectric strain gauges [18,19]) at two structure points, which are located symmetrically around the coupling DOF (see Fig. 4 and 5) with the spacing s. When I_y is constant, $T_{z,\mathrm{c}}$ can be identified with the following equation:

$$T_{z,\mathrm{c}} \approx \frac{M_{y,\mathrm{c_b}} - M_{y,\mathrm{c_a}}}{s} \tag{13}$$

which is based on Eq. (12). $M_{y,\mathrm{c_a}}$ and $M_{y,\mathrm{c_b}}$ are bending moments, corresponding to the points $\mathrm{c_a}$ and $\mathrm{c_b}$, respectively (Fig. 5). $M_{y,\mathrm{c_a}}$ and $M_{y,\mathrm{c_b}}$ are calculated with Eq. (10). When the strain responses are measured at the points $\mathrm{c_a}$ and $\mathrm{c_b}$, the bending moment at the point c can be obtained by calculating the average value:

$$M_{y,\mathrm{c}} \approx \frac{M_{y,\mathrm{c_a}} + M_{y,\mathrm{c_b}}}{2} \tag{14}$$

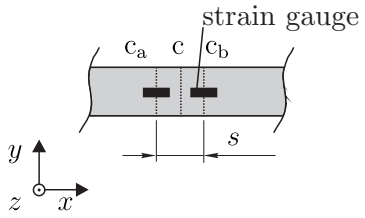

Fig. 5: The strain gauges for the interface force identification

Using the strain FRF matrix [18, 20, 21] of the structure AB the bending moment $M_{y,\mathrm{c}}$ (Eq. (14)) can be calculated with the following equation:

$$M_{y,\mathrm{c}} = \frac{1}{2}\,\frac{I_y}{e_z}\,E \begin{bmatrix} \mathbf{H}^{\mathrm{AB},\varepsilon_{xx}}_{\mathrm{c_a a}} + \mathbf{H}^{\mathrm{AB},\varepsilon_{xx}}_{\mathrm{c_b a}} & \mathbf{H}^{\mathrm{AB},\varepsilon_{xx}}_{\mathrm{c_a b}} + \mathbf{H}^{\mathrm{AB},\varepsilon_{xx}}_{\mathrm{c_b b}} \end{bmatrix} \begin{bmatrix} \mathbf{f}_{\mathrm{a}} \\ \mathbf{f}_{\mathrm{b}} \end{bmatrix} \tag{15}$$

where $\mathbf{H}^{\mathrm{AB},\varepsilon_{xx}}$ is the strain FRF matrix of the complex structure. An element of $\mathbf{H}^{\mathrm{AB},\varepsilon_{xx}}$ can be written as:

$$H^{\mathrm{AB},\varepsilon_{xx}}_{jk} = \frac{\varepsilon_{xx,\,k}}{F_j} \tag{16}$$

where $\varepsilon_{xx,\,k}$ is the normal strain in the x-direction and F_j is the excitation force. The shear force (13) can be written in a similar way as Eq. (15):

$$T_{z,\mathrm{c}} = \frac{I_y}{e_z\, s}\; E \begin{bmatrix} \mathbf{H}^{\mathrm{AB},\varepsilon_{xx}}_{\mathrm{c_b a}} - \mathbf{H}^{\mathrm{AB},\varepsilon_{xx}}_{\mathrm{c_a a}} & \mathbf{H}^{\mathrm{AB},\varepsilon_{xx}}_{\mathrm{c_b b}} - \mathbf{H}^{\mathrm{AB},\varepsilon_{xx}}_{\mathrm{c_a b}} \end{bmatrix} \begin{bmatrix} \mathbf{f}_{\mathrm{a}} \\ \mathbf{f}_{\mathrm{b}} \end{bmatrix} \tag{17}$$

Eq. (15) and (17) can be used for numerical simulations. The derivations for $M_{z,\mathrm{c}}$ and $T_{y,\mathrm{c}}$ can be performed in a similar way as for $M_{y,\mathrm{c}}$ and $T_{z,\mathrm{c}}$, respectively (Fig. 5). When the substructures are coupled with several beams (*e.g.*, a steel tower) the same procedure can be used for each coupling beam. When the interface forces are dominated by the torsional moments, the identification of bending moments and shear forces is not sufficient for accurate substructure identification.

3.3 The Identification of the substructure's FRF matrix

The coupled substructure B (Fig. 1b) can be considered as a stand-alone system that is manipulated with the excitation force $\mathbf{f}^{\mathrm{B}}$ (see Eq. (3)):

$$\mathbf{f}^{\mathrm{B}} = \begin{bmatrix} \mathbf{f}^{\mathrm{B}}_{\mathrm{c}} \\ \mathbf{f}_{\mathrm{b}} \end{bmatrix}_{n_{\mathbf{F}}} \tag{18}$$

where $n_{\mathbf{F}}$ is the number of excitation forces corresponding to the coupled substructure B. The excitation forces that excite the coupled substructure B, corresponding to the m linearly independent load steps can be collected in the matrix $\mathbf{F}^{\mathrm{B}}$:

$$\mathbf{F}^{\mathrm{B}} = \begin{bmatrix} {}_1\mathbf{f}^{\mathrm{B}} & \cdots & {}_i\mathbf{f}^{\mathrm{B}} & \cdots & {}_m\mathbf{f}^{\mathrm{B}} \end{bmatrix}_{n_{\mathbf{F}} \times m} \tag{19}$$

The responses of the structure B that correspond to the m linearly independent load steps can be written as:

$$\mathbf{U}^{\mathrm{B}} = \begin{bmatrix} {}_1\mathbf{u}_{\mathrm{c}} & \cdots & {}_i\mathbf{u}_{\mathrm{c}} & \cdots & {}_m\mathbf{u}_{\mathrm{c}} \\ {}_1\mathbf{u}_{\mathrm{b}} & \cdots & {}_i\mathbf{u}_{\mathrm{b}} & \cdots & {}_m\mathbf{u}_{\mathrm{b}} \end{bmatrix}_{n_{\mathbf{U}} \times m} \tag{20}$$

where $n_{\mathbf{U}}$ is the number of responses. For the theoretical analysis the response and excitation points correspond to the DOFs of the substructure B; therefore, $n_{\mathbf{U}}$ and $n_{\mathbf{F}}$ are equal to the number of substructure B DOFs n_{B}. The relation between $\mathbf{U}^{\mathrm{B}}$ and $\mathbf{F}^{\mathrm{B}}$ can be written as [4, 5]:

$$\mathbf{U}^{\mathrm{B}} = \mathbf{H}^{\mathrm{B}}\, \mathbf{F}^{\mathrm{B}} \tag{21}$$

where $\mathbf{H}^{\mathrm{B}}$ is the FRF matrix of the subsystem B (as a stand-alone structure). Eq. (21) is determined or over-determined when the number of linearly

independent excitation steps m is equal to or higher than n_{B} ($m \geq n_{\mathrm{B}}$) [4,5,22]. When Eq. (21) is over-determined $\mathbf{H}^{\mathrm{B}}$ can be solved using the least-squares solution of Eq. (21) [4,5]:

$$\mathbf{H}^{\mathrm{B}} = \mathbf{U}^{\mathrm{B}}\, \mathbf{F}^{\mathrm{B}\,+} \tag{22}$$

where $^+$ denotes the generalized inverse of the matrix. When m equals n_{B} the matrices $\mathbf{U}^{\mathrm{B}}$ and $\mathbf{F}^{\mathrm{B}}$ become square and the regular matrix inversion can be made. In practice, where the real structures are tested, the number of response points and excitation points (corresponding to the substructure B) is usually not the same. In this case Eq. (21) is determined or over-determined when $m \geq n_{\mathbf{F}}$.

4 The analysis of the errors

The proposed approach is based on measurements that are contaminated with errors. The measurement errors propagate in the process and lead to errors in the final results. The errors have two components, *i.e.*, systematic and random [23,24]. The systematic errors are due to the systematic effects that can be reduced by corrections when the effects are recognized and quantified [23, 24]. In this research some of the potential systematic errors were analyzed for the interface force identification (Section 6.1). The random errors can usually be evaluated through a statistical analysis. They are usually referred to as measurement noise [5, 25]. The most usual sources of measurement noise are the random influences from the measurement environment and the round-off errors in the A/D conversion [5, 25]. The effects of the random errors cannot be eliminated, but they can usually be reduced by increasing the number of observations. In general, however, the true value of a measured quantity cannot be obtained exactly. The lack of knowledge about this true value is called the uncertainty [23, 24]. In this research the uncertainty will be evaluated by statistical means. In practice it is convenient for the spread of data points around the mean values to be expressed with the standard deviation [5, 25]. When the final result is the function of several input quantities, the uncertainty of the final results depends on the uncertainty of all the inputs. When the input quantities are independent (uncorrelated), the uncertainty in the result can be calculated with the following equation [5, 25]:

$$\sigma(g(\mathbf{x})) = \sqrt{\sum_{i=1}^{n_g} \left(\frac{\partial g}{\partial x_i} \sigma(x_i) \right)^2} \tag{23}$$

where $\sigma(g(\mathbf{x}))$ is the standard deviation of the function $g(\mathbf{x})$, and $\mathbf{x}$ is a vector of the n_g input quantities x_i. $\sigma(x_i)$ is the standard deviation of x_i. Equation (23) is based on a linear assumption.

5 Case study 1

To illustrate the proposed approach the numerical simulations were made on a mass-spring-damper system (see Fig. 6). The system is assembled from the subsystems A and B, which are connected with two springs (k_4 and k_5). The mass and stiffness parameters are listed in Table 1. The system is lightly damped. The proportional-viscous-damping model was assumed, where the damping matrix was proportional to the mass ($\alpha = 10^{-5}$) and stiffness ($\beta = 10^{-7}$) matrices.

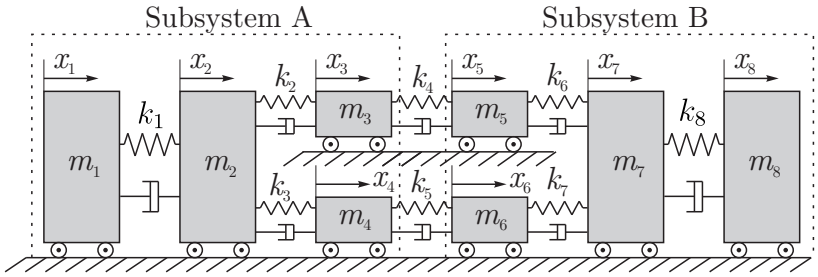

Fig. 6: The lumped dynamical system

Table 1: The mass and stiffness parameters

i	1	2	3	4	5	6	7	8
m_i[kg]	1.0	2.0	3.0	2.0	4.0	1.0	2.0	1.0
k_i[N m^{-1}]	10^7	10^7	2×10^7	10^7	2×10^7	10^7	2×10^7	2×10^7

The FRF matrix of the substructure B was identified with the procedure that was presented in Section 3. In the case 1 the calculation was made with the complete FRF matrices (no reduction was done). The responses of the system AB were calculated from the response model $\mathbf{H}^{\mathrm{AB}}$. To ensure that Eq. (21) is over-determined, five linearly independent excitation steps were made, where

Table 2: Force values at excitation steps

i	${}_if_1$	${}_if_2$	${}_if_3$	${}_if_4$	${}_if_5$	${}_if_6$	${}_if_7$	${}_if_8$
1	1	0	1	0	0	0	0	0
2	0	1	0	4	1	3	0	0
3	0	0	1	2	1	5	1	1
4	0	5	0	0	1	3	0	0
5	0	2	0	1	1	0	2	1

the structure was excited at the points 1-8. For each excitation step the excitation vector was built where the real constant values were chosen for the whole frequency range. The values of the excitation vectors are shown in Table 2.

The interface forces were identified using Eq. (6) and the FRFs of the subsystem B were identified with Eq. (22). The result of the analysis is the complete FRF matrix of the subsystem B. The results (FRFs) are plotted as accelerances [1] with a frequency resolution of 2.6 Hz. Fig. 7 shows the identified accelerance of the subsystem B between the points 8 and 6 ($\hat{A}^{\mathrm{B}}_{86}$), the true accelerance (A^{B}_{86}) and the accelerance of the structure AB, denoted as A^{AB}_{86}. The identified accelerance $\hat{A}^{\mathrm{B}}_{86}$ matches the true one A^{B}_{86}. The comparison of A^{B}_{86} and A^{AB}_{86} shows that when the subsystem B is uncoupled, its dynamical properties are significantly changed.

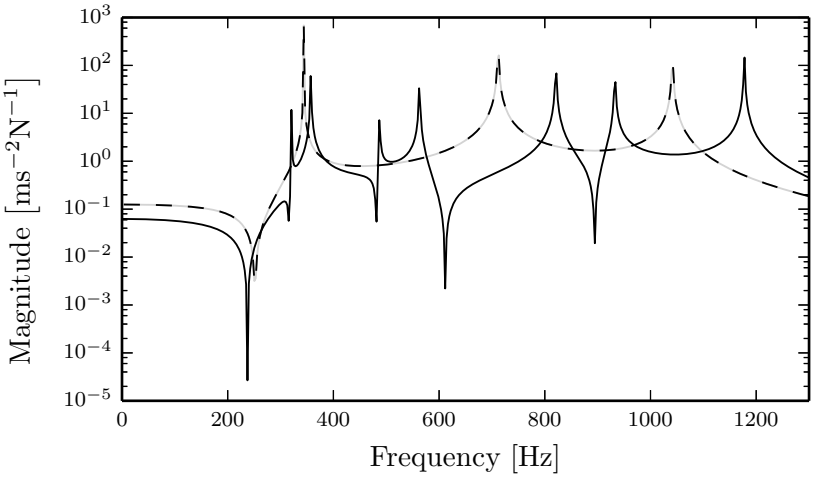

Fig. 7: The accelerance of the subsystem B (A^{B}_{86}): Identified (black - - -), True (grey —); The accelerance of the system AB (A^{AB}_{86}): (black —)

6 Case study 2

To validate the proposed approach on a continuous structure the experiment (numerical and real) was conducted on a steel, 1-m-long, free-free supported beam with a rectangular, 0.01×0.03 m^2 cross-section (Fig. 8). Only the bending modes in the plane xz are considered, which result in displacements in the z-direction and normal strains in the x-direction [14]. The beam is considered as a structure AB, which is assembled from the substructures A and B (see Fig. 8). The case study 2 includes the numerical simulations and the experimental tests.

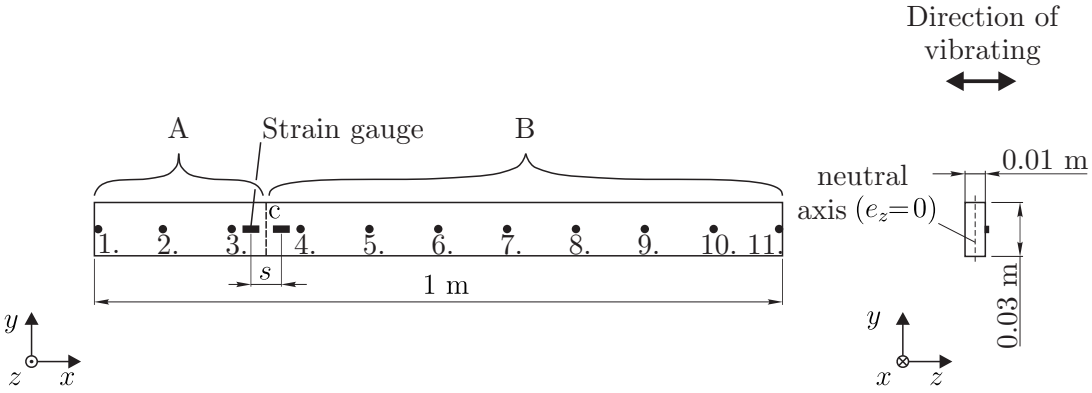

Fig. 8: The tested beam

6.1 Numerical simulations

In this section the substructure decoupling is based on the quantities (with the frequency resolution of 1 Hz) that are calculated using (FEM) harmonic analysis. The proportional hysteretic damping model was assumed with the constant damping loss factor $\eta = 8 \times 10^{-4}$.

6.1.1 The substructure identification with the pure data

The numerical simulations were made with the same quantities (motion and strain responses) as for the experimental test (Section 6.2). The structure AB was excited at the points 1 and 3 with the excitation forces. To obtain the interface forces between the substructures A and B the shear forces (T_z, c) and the bending moments (M_y, c) were calculated at the point c. The responses were calculated at the point 11. These quantities are used for the identification of the

substructure B. The sizes of the excitation (a column of $\mathbf{F}^{\mathrm{B}}$) and the response vector (a column of $\mathbf{U}^{\mathrm{B}}$) are two ($n_{\mathbf{F}} = 2$) and one ($n_{\mathbf{U}} = 1$), respectively (see Eq. (19) and (20)). To ensure that Eq. (21) is determined, two excitation steps are required. The structure excitation was made as follows: In the first and second steps the structure was excited with the unit force (a constant value over the whole frequency range) at the points 1 and 2, respectively. The results of the substructure decoupling are the FRFs of the substructure B as a stand-alone dynamical system. The input data enable the identification of the motion (translational) and moment (rotational) FRFs between the response point 11 and the excitation point c. Fig. 9 shows the accelerance of the substructure B between the response point 11 and the excitation point c ($\hat{A}^{\mathrm{B}}_{11\,\mathrm{c}}$) that was identified using the proposed approach, the true accelerance of the substructure B ($A^{\mathrm{B}}_{11\,\mathrm{c}}$) and the accelerance corresponding to the structure AB ($A^{\mathrm{AB}}_{11\,\mathrm{c}}$). The identified accelerance $\hat{A}^{\mathrm{B}}_{11\,\mathrm{c}}$ matches the true accelerance $A^{\mathrm{B}}_{11\,\mathrm{c}}$.

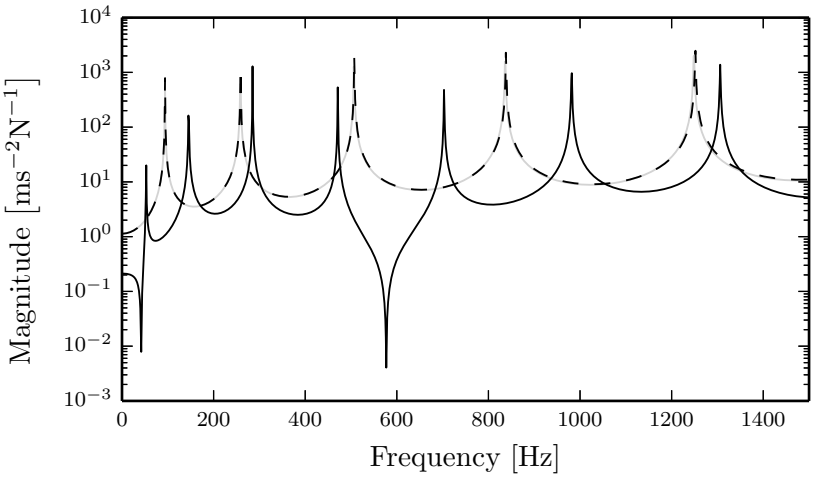

Fig. 9: The accelerances of substructure B ($A^{\mathrm{B}}_{11\,\mathrm{c}}$): Identified (black - - -), True (grey —); The accelerance of the structure AB ($A^{\mathrm{AB}}_{11\,\mathrm{c}}$): (black —)

6.1.2 Analysis of the systematic errors

In Section 6.2 (real experiment) the bending moments and shear forces of the real beam are identified using the procedure that was presented in Section 3.2.2. To test the sensitivity of the final results to potential systematic errors the analysis of the spacing between the strain gauges (Section 3.2.2) and analysis

of the incorrect sensitivity (due to inappropriate attaching) of the strain gauge was made.

As can be seen from Section 3.2.2 the spacing between the strain gauges is important for the accuracy of the interface force identification and the results of the substructure decoupling. To analyze the influence of the spacing s (Eqs. (14) and (13)) a series of decoupling procedures was made where s varied from 20 mm to 60 mm. The accelerances of the decoupled substructure B $\hat{A}^{\mathrm{B}}_{11\,\mathrm{c}}$ that are based on the 20-mm and 60-mm spacings are shown in Fig. 10 together with the true accelerance $A^{\mathrm{B}}_{11\,\mathrm{c}}$. While the relatively large spacings ($s = 60$ mm) result in the frequency shifts and magnitude variations, the 20-mm spacing does not have a significant effect on the final results.

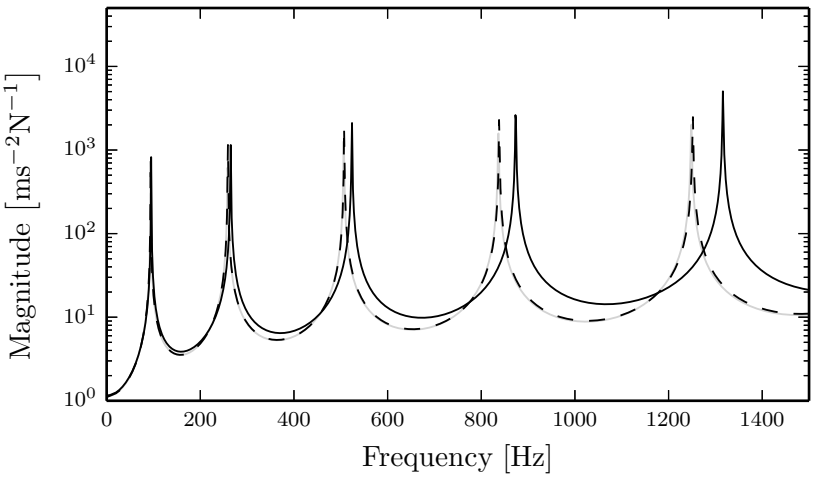

Fig. 10: The identified accelerance of the substructure B ($\hat{A}^{\mathrm{B}}_{11\,\mathrm{c}}$): The spacing $s = 60$ mm (black —), $s = 20$ mm (black - - -); and the true $A^{\mathrm{B}}_{11\,\mathrm{c}}$ (grey —)

If the strain gauges are not attached in accordance with the producer's instructions the sensitivity of the strain gauge is changed [19, 20]. To analyze this effect, a simulation was made, where the sensitivity of the sensor at the point $\mathrm{c_b}$ was reduced by 20 %. Due to the reduced strain gauge-sensitivity the identified FRF increased by a factor that was (approximately) constant over the whole frequency range. The 20 %-sensitivity reduction resulted in a less than 13 % increase in the identified accelerance and moment accelerance of the substructure B.

6.1.3 The uncertainty propagation analysis of the decoupling technique

The goal of the uncertainty propagation analysis is to research how the uncertainties of the input quantities affect the final result $\mathbf{H}^{\mathrm{B}}$. The uncertainty propagation analysis was made with Monte Carlo simulations. It is assumed that the uncertainties of the input quantities are specified in terms of confidence intervals at the 95 % level (95 % of the generated input quantities were inside the confidence intervals). The confidence intervals of the input quantities $\mathbf{F}^{\mathrm{B}}$ and $\mathbf{U}^{\mathrm{B}}$ were proportional to the magnitudes with the factor 0.1 %. A total of 1000 simulations were made. For every Monte Carlo simulation a random input quantity was generated for every frequency point. The distribution of the simulated input quantities is Gaussian. The confidence intervals of the calculated substructure's FRF magnitudes (the results of Monte Carlo simulations) were defined at the 95 % level (95 % of the calculated data was inside the confidence intervals).

The convergence check of the Monte Carlo simulations was made by plotting the mean values and standard deviations of the calculated FRFs magnitudes against the number of simulations. As an example, the convergence check is shown for simulated accelerances $\tilde{A}^{\mathrm{B}}_{11\mathrm{c}}$ at the frequency 851 Hz in Fig. 11. Fig. 11 shows, that the number of simulations is sufficient to achieve the convergence.

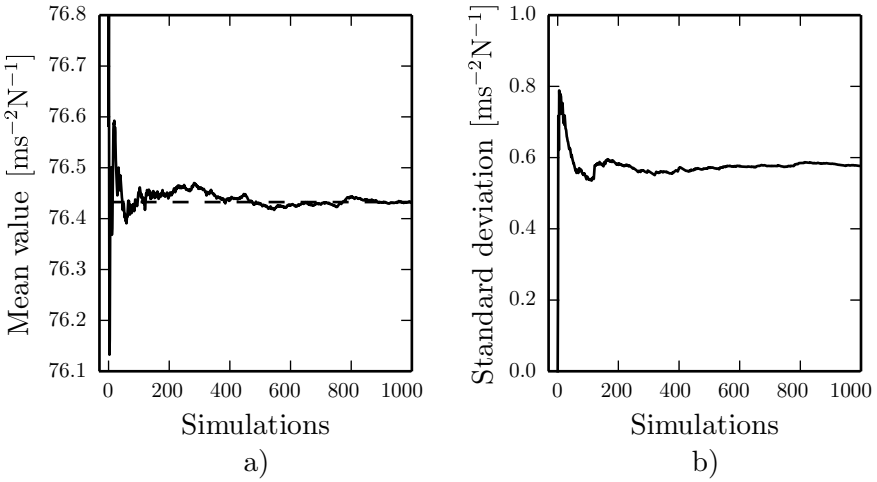

Fig. 11: Magnitude of accelerance $\tilde{A}^{\mathrm{B}}_{11\mathrm{c}}$ at the frequency 851 Hz: a) Mean values (—) and true value (– –) ; b) Standard deviations

The results of the analysis are shown as the mean accelerance of the substructure B (between the structure points 11 and c) together with the confidence intervals in Fig. 12 and as the ratio between the confidence interval and the mean accelerance in Fig. 13. Fig. 12 and Fig. 13 show that the uncertainties are magnified significantly around the resonance peaks of the substructure B and the structure AB. The numerically calculated natural frequencies of the complex structure occur at 53 Hz, 145 Hz, 285 Hz, 471 Hz, 703 Hz, 982 Hz and 1306 Hz. The numerically calculated natural frequencies of the substructure B occur at 94 Hz, 259 Hz, 507 Hz, 838 Hz and 1252 Hz. The analysis of the simulation results also showed that the magnitude distribution of a substructure's B FRF at a single frequency point is not Gaussian over the whole frequency range. The distribution is not normal at the points where the uncertainties are propagated the most. At these points the mean value of the substructure's FRF magnitude does not match the true values. These facts indicate nonlinear effects; therefore, the calculated confidence intervals at these frequency points are not reliable.

The results of the uncertainty propagation analysis show that significant errors can occur around the natural frequencies of the structure AB and the spurious peaks around the natural frequencies of the substructure B.

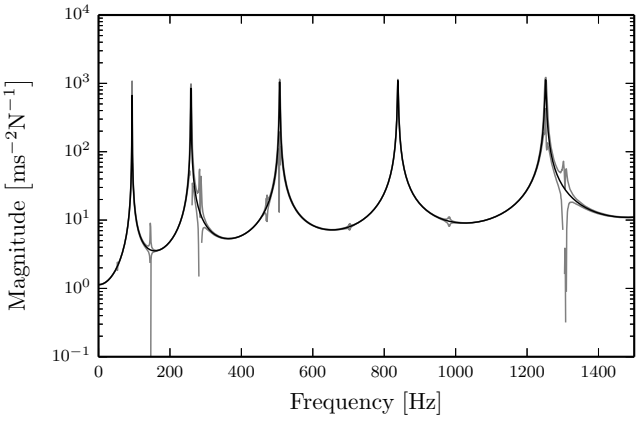

Fig. 12: The accelerance of the substructure B $\hat{A}^{\mathrm{B}}_{11\,\mathrm{c}}$: Identified (black), identified with the confidence intervals (grey)

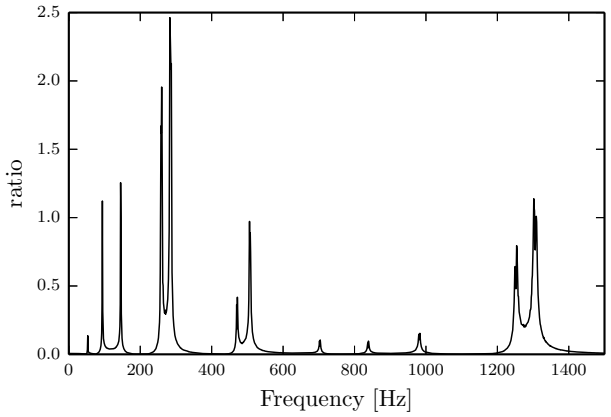

Fig. 13: Ratio between the confidence interval and mean accelerance ($\hat{A}^{\mathrm{B}}_{11\,\mathrm{c}}$)

6.2 Experimental testing

This section introduces the results of the experimental testing on the real beam (Fig. 14). The free-free boundary conditions of the beam were achieved by suspending the structure from thin ropes. During the experimental testing the structure was excited with a modal hammer (B&K Type 8206-002). The strain responses were measured with two piezoelectric strain gauges (PCB 740B02 [19]), which were attached symmetrically around the point c. The attaching of the the strain gauges is shown in Fig. 8 and 14. In accordance with the error analysis of the strain-gauges spacing in Section 6.1.2, the spacing 20 mm was chosen. The motion responses were measured at point 11 with the piezoelectric accelerometer (B&K Type 4517-002). The identification of the shear forces ($T_{z,\mathrm{c}}$) and the bending moments ($M_{y,\mathrm{c}}$) was made with Eqs. (13) and (14), respectively. To compare the identified interface forces with the calculated ones using the validated finite-element (FE) model the results are plotted as the FRFs between the shear force (bending moment) and the external excitation force. Fig. 15 shows the FRF between $T_{z,\mathrm{c}}$ and the excitation point 1. FRF between $M_{y,\mathrm{c}}$ and excitation point 1 is shown in Fig. 16. The frequency resolution of the quantities that are plotted in this section is 0.1 Hz. Fig. 15 and 16 show that the identified interface forces match the calculated ones well.

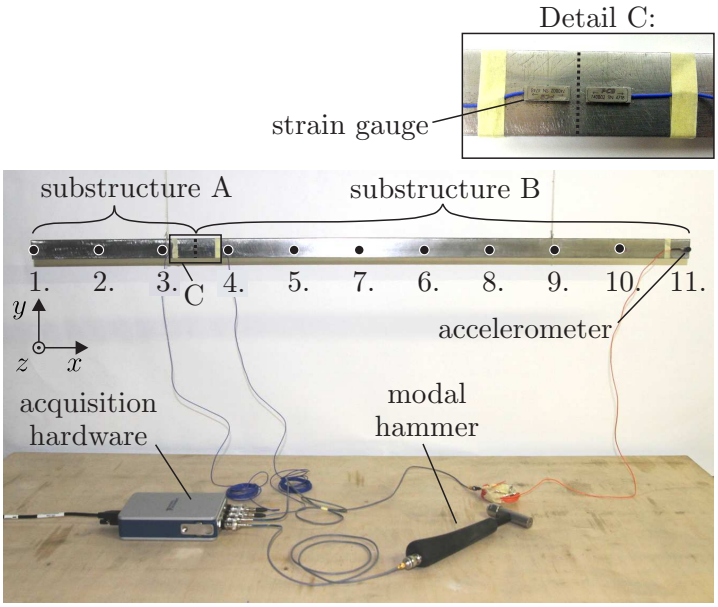

Fig. 14: The experimental testing

Table 3: The natural frequencies of the tested beam

r	ω_r	direction
1	52.7 Hz	z axis
2	144.6 Hz	z axis
3	157.6 Hz	y axis
4	282.9 Hz	z axis
5	428.9 Hz	y axis
6	467.5 Hz	z axis
7	697.7 Hz	z axis
8	833.3 Hz	y axis
9	928.9 Hz	torsional
10	972.2 Hz	z axis
11	1292.6 Hz	z axis
12	1363.3 Hz	y axis

In this experiment the size of the excitation vector ($n^{\mathbf{F}} = 2$) and the response vector ($n^{\mathbf{U}} = 1$) is the same as for the numerical testing (Section 6.1). The linearly independent excitation steps were made in the same way as for the numerical simulations. The measured responses, (identified) shear forces and bending moments were used to identify the substructure B FRFs. The identified accelerance $\hat{A}^{\mathrm{B}}_{11\,\mathrm{c}}$ (between the points 11 and c) is plotted together with the measured one (Fig. 17), where the free-free supported beam with the length L=750 mm was tested. The identified moment accelerance $\hat{A}^{M,\mathrm{B}}_{11\,\mathrm{c}}$ is plotted together with the calculated one (from the validated FE model) in Fig. 18. Fig. 17 and 18 show that the experimental results match the calculated ones well. The main reasons for the discrepancies are the consequences of the measuring errors. Some of the discrepancies were predicted with the uncertainty propagation analysis (Section 6.1.3) *i.e.*, the relatively high discrepancies around the resonance peaks of the substructure B (*e.g.*, 144.6 Hz, 282.9 Hz,1292.6 Hz). The spurious peaks around 157.6 Hz, 428.9 Hz and the discrepancy around 833.3 Hz occur at the natural frequencies of the beam's (structure AB) mode shapes in the y-direction, due to the transverse sensitivity of the sensors. The discrepancies around 928.9 Hz occur due to cross-axis sensitivity of the strain sensors to the shear strains at the torsional mode shape. The natural frequencies of the real beam are evident from Table 3 and were identified from the accelerances that were measured in the directions z and y (Fig. 14). The results of the experimental testing show the validity of the proposed approach.

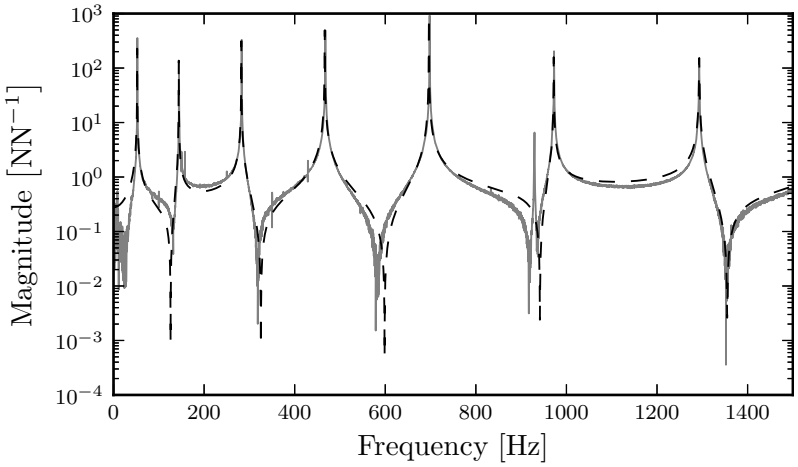

Fig. 15: The FRF between the shear force and the excitation force: Identified (grey —) and calculated (black - - -).

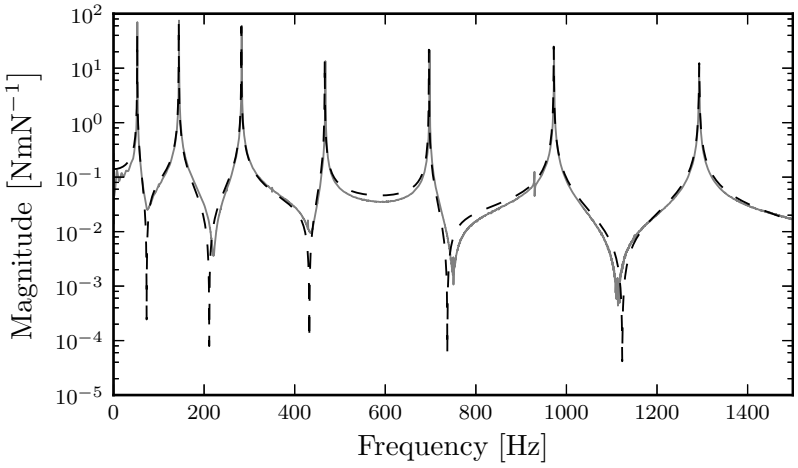

Fig. 16: The FRF between the bending moment and the excitation force: identified (grey —) and calculated (black - - -).

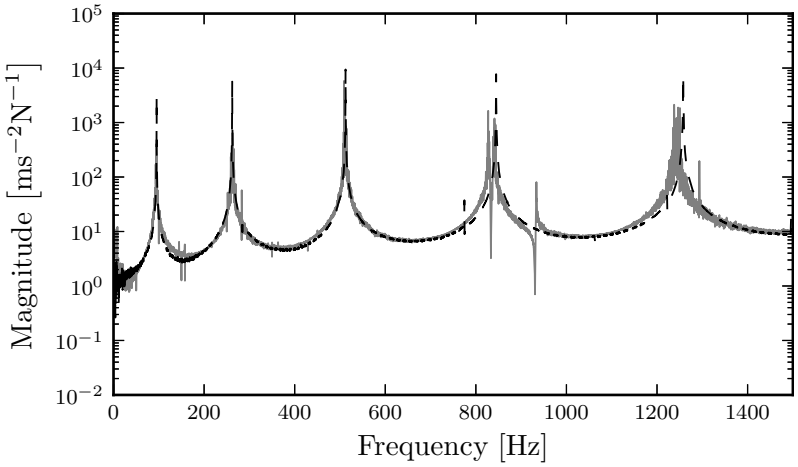

Fig. 17: The accelerance of the substructure B ($A^{\mathrm{B}}_{11\,\mathrm{c}}$): Identified (grey —) and measured for the 0.75-m-long beam (black - - -)

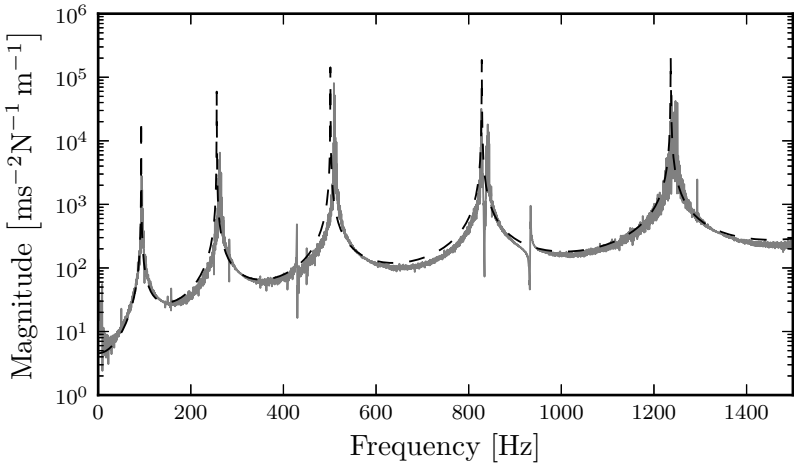

Fig. 18: The moment accelerance of the substructure B ($A^{M,\mathrm{B}}_{\mathrm{c}\,11}$): identified (grey —) and calculated (black - - -)

7 Conclusion

This research is focused on substructure-decoupling techniques. The result of substructure-decoupling techniques are the FRFs of the unknown substructure as a stand-alone structure (the complex structure is divided into the unknown and the remaining substructure). A drawback of the current substructure decoupling techniques is that the response model of the remaining substructure is required. In this article a new approach is introduced that does not require the response model of the remaining substructure. The proposed approach is based on an experimental identification of the interface forces. The interface force identification was considered on systems with spring- and beam-like coupling elements. The first type of systems were considered for an illustration of the proposed approach and the second to show the practical applications for real structures (many real structures are assembled from beam-like structures). The identified interface forces, measured responses and the excitation forces can be used for the identification of the substructure FRFs.

The proposed approach was validated on a mass-spring-damper system and a beam structure. The numerical simulations on the mass-spring-damper system showed that the identified FRFs of the subsystem match the true FRFs. The beam tests included numerical simulations and experimental testing. The results of the numerical simulations showed that the identified FRFs of the substructure match the true ones well. The numerical simulations also included the systematic- and random-error analysis. The error analysis on the beam case showed that the relatively small random error is significantly magnified in the FRFs of the substructure. However, the analysis of the spacing between the strain gauges and the analysis of the strain gauge's sensitivity change (due to inappropriate mounting) showed that these system errors do not affect the substructure's FRFs significantly. The experimental testing showed that the identified accelerances and moment accelerances correspond to the calculated values.

Acknowledgement

The operation was partially Financed by the European Union, European Social Fund.

References

[1] N. M. N. Maia, J. M. M. Silva, Theoretical and Experimental Modal Analysis, Research studies press Ltd., Baldock, Hertfordshire, England, 1997.

[2] J. He, Z. Fu, Modal Analysis, Butterworth-Heinemann, Oxford, England., 2001.

[3] D. de Klerk, D. J. Rixen, S. N. Voormeeren, General Framework for Dynamic Substructuring: History, Review, and Classification of Techniques, AIAA Journal 46 (2008) 1169–1181.

[4] P. Sjovall, T. Abrahamsson, Substructure system identification from coupled system test data, Mechanical Systems and Signal Processing 22 (1) (2008) 15 – 33.

[5] S. Voormeeren, D. Rixen, Substructure decoupling techniques - a review and uncertainty propagation analysis, in: Proceedings of the International Modal Analysis Conference IMAC-XXVII, Orlando, Florida, USA, SEM, 2009.

[6] S. Voormeeren, D. Rixen, A family of substructure decoupling techniques based on a dual assembly approach, Mechanical Systems and Signal Processing 27 (0) (2012) 379 – 396.

[7] D. Cloutier, P. Avitabile, Investigation on the use of various decoupling approaches, in: Proceedings of the 28 International Modal Analysis Conference (IMAC XXVIII), Jacksonville, Florida, Society for Experimantal Mechanics Inc., 2010, pp. 679–687.

[8] W. D'Ambrogio, A. Fregolent, Direct decoupling of substructures using primal and dual formulation, in: Proceedings of the 27 International Modal Analysis Conference (IMAC XXIX), SEM, 2011, pp. 47–76.

[9] P. Ind, D. Ewins, Impedance based decoupling and its application to indirect modal testing and component measurement: a numerical investigation, in: Proceedings of 21th International Modal Analysis Conference, Kissimmee, FL, Society for Experimental Mechanics, Bethel, CT, 2003, 2003.

[10] W. D'Ambrogio, A. Fregolent, Promises and pitfalls of decoupling procedures, in: Proceedings of the 26 International Modal Analysis Conference (IMAC XXVI), Orlando, Florida, 2008.

[11] S. Voormeeren, D. Rixen, A dual approach to substructure decoupling techniques, in: Proceedings of the 28th International Modal Analysis Conference IMAC-XXVIII, Jacksonville, Florida USA, Society for Experimantal Mechanics Inc., 2010, pp. 601–616.

[12] D. J. Ewins, Modal testing: Theory and Practice, Research studies press Ltd., Baldock, Hertgordshire, England, 1984.

[13] W. Heylen, S. Lammers, P. Sas, Modal Analysis Theory and Testing, Katholieke Universiteit Leuven, Haverlee, Belgium, 2007.

[14] S. S. Rao, Mechanical Vibrations, Prentice Hall, Upper Saddle River, NJ., 2010.

[15] M. Kutz, Mechanical Engineers' Handbook, A Wiley-Interscience publication, Wiley, 1998.

[16] K. Washizu, Variational Methods in Elasticity and Plasticity, 01, Elsevier Science & Technology, 1974.

[17] R. Burden, J. Faires, Numerical Analysis, Brooks/Cole, Cengage Learning, 2011.

[18] T. Kranjc, J. Slavič, M. Boltežar, The mass normalization of the displacement and strain mode shapes in a strain experimental modal analysis using the mass-change strategy, Journal of Sound and Vibration 332 (26) (2013) 6968 – 6981.

[19] J. J. Dosch, Piezoelectric strain sensor, in: Proceedings of the International Modal Analysis Conference IMAC, SEM, Bethel, CT, United States, 1999.

[20] T. Kranjc, J. Slavič, M. Boltežar, A comparison of strain and classic experimental modal analysis, Journal of Vibration and Control , Published online April 29, 2014.

[21] L. Yam, T. Leung, D. Li, K. Xue, Theoretical and experimental study of modal strain analysis, Journal of Sound and Vibration 191 (2) (1996) 251 – 260.

[22] D. Čelič, M. Boltežar, The influence of the coordinate reduction on the identification of the joint dynamic properties, Mechanical Systems and Signal Processing 23 (4) (2009) 1260 – 1271.

[23] G. R. Semyon, Evaluating Measurement Accuracy, Springer, New York, Dordrecht, Heidelberg, London, 2010.

[24] H. Coleman, W. Steele, Experimentation, Validation, and Uncertainty Analysis for Engineers, John Wiley & Sons, Inc., New York, 2009.

[25] S. Voormeeren, D. de Klerk, D. Rixen, Uncertainty quantification in experimental frequency based substructuring, Mechanical Systems and Signal Processing 24 (1) (2010) 106 – 118.